CrystEngComm

ROYAL SOCIETY
OF **CHEMISTRY**

PAPER
Duane Choquesillo-Lazarte *et. al.*
Seeking new polymorphs in pharmaceutical cocrystals: focus
on furosemide–ethenzamide

Check for updates

Seeking new polymorphs in pharmaceutical cocrystals: focus on furosemide–ethenzamide

Estephany Muñoz-Hernández, [ID] [ab] Carolina Alarcón-Payer, [ID] [c] Antonio Frontera, [ID] [d] Rafel Prohens, [ID] [e] Rafael Barbas, [ID] [f] Francisco Javier Acebedo-Martínez, [ID] *[a] Alicia Domínguez-Martín [ID] [b] and Duane Choquesillo-Lazarte [ID] *[a]

Polymorphism remains a critical challenge in the pharmaceutical industry due to its profound impact on the physicochemical and biopharmaceutical properties of active pharmaceutical ingredients (APIs). While pharmaceutical multicomponent materials (PMMs) such as cocrystals were initially believed to mitigate polymorphic risks through stabilization *via* non-covalent interactions, while modulating the properties of different APIs, recent studies have revealed a growing number of polymorphic PMMs, highlighting the need for targeted screening and structural understanding of these materials. In this work, we report the discovery and selective synthesis of a novel polymorph of the furosemide–ethenzamide (**FUR**–**ETZ**) cocrystal through kinetic crystallization *via* fast solvent evaporation. Solid-state characterization confirmed the formation of a polymorph with morphotropic packing relative to the known form, despite maintaining similar molecular conformation and hydrogen bonding motifs. Crystal structure analysis revealed that **form II** exhibits a lateral layer shift and increased surface polarity, resulting in enhanced aqueous solubility and a slightly higher melting point. In contrast, **form I** was shown to be thermodynamically more stable, both in dry and aqueous environments, as supported by lattice energy calculations and competitive slurry experiments. These findings underscore the relevance of polymorph screening in PMMs and demonstrate how subtle variations in crystal packing can critically influence the stability and performance of pharmaceutical cocrystals.

Introduction

Pharmaceutical Multicomponent Materials (PMMs)—such as salts and cocrystals—have emerged over recent decades as pivotal strategies to enhance the physicochemical and pharmacokinetic properties of active pharmaceutical ingredients (APIs), particularly solubility and permeability.[1–5] These systems exploit non-covalent interactions (mainly hydrogen bonding and π–π stacking) to produce novel solid-state forms with modulated physicochemical properties.[6–8] However, apart from their exciting advantages, PMMs also introduce new complexities that

necessitate careful investigation and control, the most relevant being polymorphism.[9,10]

While polymorphism in single-component APIs has been extensively investigated,[11–14] the study of polymorphism in PMMs, although increasingly addressed in recent years, remains comparatively less developed.[15] Initially, cocrystallization was reported as a strategy to eliminate polymorphic risk, as the non-covalent interactions would stabilise and discard polymorphic transitions.[10,16,17] However, this hypothesis was quickly discarded by the appearance of numerous examples of cocrystal polymorphs.[18–23] Indeed, population analyses show that polymorphism in cocrystals may exceed that in single-component systems, underscoring the need for dedicated research.[24–28] Additionally, regulatory agencies rigorously control solid-state forms, and PMMs are not an exception. Therefore, they must be reproducibly synthesized, accurately characterized, and stable through processing and storage to ensure consistent bioavailability and regulatory acceptance. Failure to detect and control polymorphism and polymorphic transitions can lead to product inconsistency, manufacturing stoppages, and noncompliance with regulatory standards.[29–32]

Polymorphic outcome is fundamentally dictated by nucleation dynamics, crystal growth rates, and the metastable-to-stable transitions.[33–37] Therefore, a systematic exploration of

[a] *Laboratorio de Estudios Cristalográficos, IACT-CSIC, Avda. de las Palmeras 4, 18100 Armilla, Spain. E-mail: duane.choquesillo@csic.es*
[b] *Department of Inorganic Chemistry, Faculty of Pharmacy, University of Granada, 18071 Granada, Spain*
[c] *Servicio de Farmacia, Hospital Universitario Virgen de las Nieves, 18014 Granada, Spain*
[d] *Departament de Química, Universitat de les Illes Balears, Crta. de Valldemossa km 7.5, 07122 Palma, Spain*
[e] *Laboratory of Organic Chemistry, Faculty of Pharmacy and Food Sciences, University of Barcelona, Avda. Joan XXIII, 08028 Barcelona, Spain*
[f] *Unitat de Polimorfisme i Calorimetria, Centres Científics i Tecnològics, Universitat de Barcelona, Baldiri Reixac 10, 08028 Barcelona, Spain*
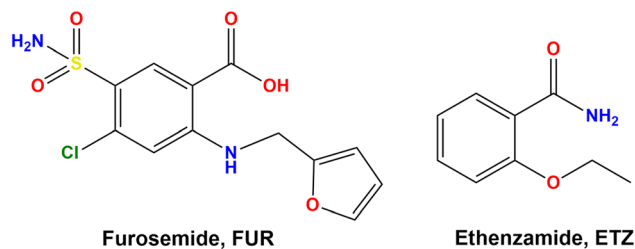
Fig. 1 Chemical formula of FUR and ETZ active pharmaceutical ingredients.

synthetic conditions is essential to map the polymorphic landscape of a given PMM system and establish robust protocols to reproducibly generate only desired forms.[38–40]

In this work, we present a novel polymorph of the furosemide (FUR)–ethenzamide (ETZ) (Fig. 1) cocrystal (**FUR–ETZ**), already reported by our group,[41] (CCDC No. 2114160), as a model to systematically explore polymorphism in PMMs. Our objectives are to (1) explore varied crystallization methods to obtain a pure bulk phase of a novel polymorph of the FUR–ETZ system, (2) perform a complete solid-state characterization and (3) assess the impact of the crystal structure on key physicochemical behaviours of the novel polymorph. By doing so, we underscore the importance of integrating polymorphism-focused screening during the development of PMMs, improving product consistency and regulatory compliance.

Materials and methods

Materials

FUR, ETZ and solvents were purchased from Sigma-Aldrich (purity >98%, Sigma-Aldrich, St. Louis, MO, USA) and were used as received.

Solvents used: acetonitrile (ACN), benzene (BZN), butanone (BNA), butyl glycolate (BGL), chlorobenzene (CLB), dichloromethane (DCM), ethanol (EOH), ethyl acetate (ETA), hexane (HEX), isopropanol (ISP), methanol (MET), *n*-butanol (BUT), tetrahydrofuran (THF) and tetrahydropyran (THP).

Buffer solutions were prepared as follows: for the 0.01 M phosphate-buffered saline (PBS, pH 6.8), 0.02 g of KCl, 0.144 g of sodium phosphate dibasic (Na_2HPO_4), 0.08 g of sodium chloride (NaCl), and 0.02 g of potassium phosphate monobasic (KH_2PO_4) were dissolved in 1 L of Milli-Q water. For the 0.02 M potassium chloride (KCl) solution (pH 1.2), 1.491 g of KCl was dissolved in 1 L of Milli-Q water. Finally, 37% hydrochloric acid (HCl) and 1 M HCl were added gradually until the solutions reached pH values of 6.8 and 1.2, respectively.

Procedure for cocrystal synthesis

Form I: mechanochemical synthesis. Form I was obtained *via* liquid-assisted grinding (LAG) using a RETSCH MM2000 ball mill, following the methodology reported by our group in a previous study.[41]

Form II: fast solvent evaporation. Form II was obtained *via* fast precipitation of a 1 : 1 stoichiometric solution prepared by dissolving 0.5 mmol of ETZ (82 mg) and 0.5 mmol of FUR (165 mg) in 60 mL of EOH. The solvent was completely removed under reduced pressure using a rotary evaporator at 40 °C and 20 rpm, obtaining a crystalline precipitate.

Single crystals of **form II** were obtained by slow solvent evaporation of EOH-saturated solutions prepared by dissolving the crystalline precipitate obtained *via* fast. Good quality single crystals appeared after 2 days of slow evaporation at room temperature.

Characterization techniques

Powder X-ray diffraction. Powder X-ray diffraction (PXRD) patterns were recorded at room temperature on a Bruker D8 Advance Series II Vario diffractometer (Bruker AXS, Karlsruhe, Germany), equipped with a Ge(111) primary monochromator and a LYN-XEYE fast silicon strip detector. Data were collected in transmission geometry between Mylar foils using Cu Kα₁ radiation, with the generator operating at 40 kV and 40 mA. The angular range was 5–50° (2θ) with a step size of 0.01° (2θ), giving a total measurement time of 60 min.

Single-crystal X-ray diffraction. A Bruker D8 Venture diffractometer (Bruker AXS, Karlsruhe, Germany) with Cu Kα radiation (λ = 1.54178 Å) was used to obtain the Single-crystal X-ray diffraction (SCXRD) data at room temperature. Crystals were mounted under inert conditions using perfluoropolyether oil as a protective medium. Diffraction data were processed using the APEX4 (ref. 42) software while Olex2 (ref. 43) was used to solve the crystal structures. This was done by intrinsic phasing and refined by full-matrix least-squares on F^2. All non-hydrogen atoms were refined anisotropically. Hydrogen atoms were located from difference Fourier maps and treated as riding on their parent atoms, with isotropic displacement parameters set at 1.2 or 1.5 times those of the corresponding atoms. Structural visualization and graphical representations were generated using Mercury,[44] and Olex2.[43] CIFs can be found in the Cambridge Structural Database (CSD) under CCDC deposition number 2489369.

Theoretical methods

Periodic boundary condition calculations. The thermodynamic stability of the two polymorphs was evaluated by calculating their respective lattice energies using periodic boundary condition (PBC) calculations. These calculations were performed with the DMol3 software, as implemented in the Materials Studio package.[45] The PBE exchange–correlation functional was used in conjunction with the double numerical with polarization (DNP) basis set.[46] To ensure high-quality results, a supercell containing 16 molecules (8 of each coformer, FUR and ETZ) was constructed for each polymorph. The lattice energy for each structure was determined by comparing the total energy of the optimized supercell with the sum of the energies of the unbound constituent molecules.

Quantum chemical calculations on dimers. Quantum chemical calculations were performed on representative dimers extracted from the single-crystal X-ray structures. All dimer calculations, including the computation of molecular electrostatic potential (MEP) surfaces, quantum theory of atoms in molecules (QTAIM) analysis, and non-covalent interaction (NCI) plot analysis, were carried out using the Gaussian 16 program[47] at the PBE0-D3/def2-TZVP level of theory.[48–50] This functional and basis set combination is well-suited for the accurate description of noncovalent interactions.

The dimerization energies were corrected for basis set superposition error (BSSE) using the standard counterpoise method.[51] The QTAIM[52] and NCIplot[53] analyses, which provide a quantitative and qualitative description of bonding and noncovalent interactions, respectively, were performed with the AIMAll program.[54]

Fourier-transform infrared spectroscopy

Fourier-transform Infrared (FTIR) analysis was performed using a Hyperion 3000 instrument (Bruker Corporation, Massachusetts, USA) equipped with a single-reflection diamond crystal platinum ATR unit. Data were collected in the range of 4000 to 400 cm^{-1} with a resolution of 4 cm^{-1}, and operated with OPUS software.

Thermal analysis

Differential scanning calorimetry (DSC) analysis was carried out using a Mettler-Toledo DSC-822e calorimeter. Measurements were conducted in 40 μL aluminum crucibles, under a dry nitrogen atmosphere with a flow of 50 mL min^{-1} and a heating rate of 10 °C min^{-1}. The instrument was calibrated with indium of 99.99% purity (melting point: 156.3 °C; ΔH: 28.73 J g^{-1}).

Thermodynamic stability

The thermodynamic stability of the solid forms was evaluated under accelerated ageing conditions. Approximately 200 mg of each sample was placed in a watch glass and stored at 40 °C and 75% relative humidity in a Memmert HPP110 climate chamber (Memmert, Schwabach, Germany). The integrity of the solids under the above-mentioned conditions was periodically monitored using PXRD for 2 months.

Stability under aqueous conditions was also examined through slurry experiments. An excess amount of each solid was added to 1 mL of either (1) 0.02 M KCl buffer at pH 1.2 or (2) 0.01 M PBS buffer at pH 6.8. The suspensions were stirred for 24 hours at 25 °C in sealed vials. Afterwards, the solids were recovered, filtered, dried, and characterized by PXRD.

Polymorph competitive analysis

The transformation behaviour of **FUR–ETZ** polymorphs was investigated through slurry experiments. Separated slurries were carried out for each time point (1, 2, 4, 15 days) by suspending either 10 mg of **form I**, 10 mg of **form II**, or a 1:1 physical mixture (10 mg of each polymorph) in 500 μL of hexane. The suspensions were stirred at 25 °C in sealed vials. At each time point, the solids were then recovered, filtered, dried, and analysed via PXRD.

Solubility analysis

The solubility studies were undertaken following the shake-flask method[55] in KCl pH 1.2 and PBS pH 6.8. Saturated solutions of **form I**, **form II**, FUR and ETZ were prepared by adding an excess of solid to 10 mL of each buffer. After 24 hours of stirring at 25 °C, the solutions were filtered through 0.22 μm syringe filters, diluted to achieve a measurable concentration and analysed via high-performance liquid chromatography (HPLC).

HPLC studies were performed using a HPLC Agilent 1200 series and a C18 column (4.6 mm × 150 mm, 4 μm particle size, Phenomenex) set at 40 °C. The mobile phase consisted of (a) MilliQ water with 0.1% formic acid and (b) acetonitrile (purity >99%, Sigma-Aldrich, St. Louis, MO, USA). The mobile phase was used in an isocratic mode with an 80:20 ratio and 1 mL min^{-1} of flow rate, along with 10 μL of sample injected. The solubility of the samples was evaluated at 244 and 276 nm, maximums of absorbance of ETZ and FUR, respectively and expressed in mg mL^{-1}.

Results and discussion

Polymorph screening

The initial polymorph screening of the **FUR–ETZ** system was carried out using LAG, a well-established technique for the rapid and effective discovery of polymorphic forms.[56,57] One of the core strategies in polymorph screening via LAG is solvent variation, as different solvents can stabilize different supramolecular synthons or intermediate species.[58–60] To explore this, a multi-solvent LAG screening was performed using a wide range of solvents (Fig. S1) under two reaction times (2 and 30 minutes), aiming to identify both kinetically accessible and thermodynamically stable polymorphs.

As expected, after 30 minutes of milling, the known **form I** was consistently obtained in MET. In contrast, other solvents led to the formation of physical mixtures where **form I** coexisted with unreacted APIs and, in several cases, an unreported material. However, the composition of the mixtures varied significantly depending on the solvent, and despite testing a wide range of solvents, the unknown material could not be isolated as a pure phase suitable for solid-state characterization.

Short LAG experiments (2 minutes) typically yielded mixtures containing the unknown material and **form I**, with the novel phase being more dominant. In certain solvents, only the new material and unreacted APIs were observed, consistent with a mechanism in which FUR and ETZ first assemble into a metastable phase kinetically favoured, which subsequently converts into **form I** over time. However, the frequent coexistence of multiple phases, regardless of milling time, also suggests a complex transformation pathway

involving either a slow conversion process or a dynamic equilibrium, where unreacted APIs remain involved. These factors make it difficult to isolate the unknown material in pure form using LAG alone.

To overcome these limitations and stabilize the metastable phase, we considered a less energetic kinetic approach: Fast solvent evaporation. This method is well-documented for its ability to trap kinetically favoured forms before they convert to thermodynamic products.[61,62] Unlike LAG, which involves continuous mechanical energy input, rapid solvent evaporation provides a more controlled environment where crystallization occurs during solvent removal, allowing metastable phases to nucleate and grow before rearrangement or transformation can occur.[63,64] Fast solvent evaporation was performed with EOH, chosen both because the novel material predominantly appeared in EOH during LAG screening and because of its low boiling point and low toxicity, which make it particularly suitable for this method. Fast evaporation of saturated equimolar solutions of FUR and ETZ yielded crystalline precipitates that were characterized by PXRD, confirming the formation of a pure bulk phase of the novel form (Fig. 2).

The contrast observed between LAG and solvent evaporation highlights the importance of combining complementary techniques for polymorph screening to maximize the number of accessible forms—whether thermodynamically stable or kinetically favoured.

Although a novel PXRD pattern is observed, at this stage, we are not able to confirm the formation of a polymorph of the system **FUR–ETZ**. Complementary studies *via* FT-IR revealed significant shifts in the vibrational bands corresponding to the functional groups of FUR and ETZ, particularly in regions associated with N–H, O–H, and C=O stretching modes. Table 1 shows the most relevant signals in FT-IR of the two polymorphs found and the shifts when compared with the APIs. These changes are indicative of new intermolecular interactions, likely involving hydrogen bonding, π–π stacking, and dipole–dipole interactions. Such shifts in IR absorption bands suggest that the molecular

Table 1 FT-IR signals (cm^{-1}) of **FUR–ETZ** polymorphs and the parent APIs

Compound	$v(NH_2)$ sulfonamide	$v(NH)$ secondary amine	$v(C=O)$ carboxyl	$v(S=O)$ sulfonamide
Form I	(as) 3438 (s) 3291	3285	1670	(as) 1339 (s) 1154
Form II	(as) 3444 (s) 3274	3185	1674	(as) 1344 (s) 1166
FUR	(as) 3400 (s) 3351	3285	1670	(as) 1328 (s) 1139
ETZ	—	3168	1644	—

environment has changed, consistent with the formation of a cocrystal. Moreover, the absence of signals related to hydration or solvation, along with the consistent observation of this phase across the LAG experiments in different solvents, supports the exclusion of a solvate and favours the identification of a new cocrystal polymorph—hereafter referred to as **form II**.

The recrystallisation of **form II**, *via* slow solvent evaporation of saturated solutions in EOH, allowed the obtention of suitable crystals for SCXRD analysis, which confirmed our hypothesis. Additionally, the crystal structure of **form II** provides a simulated PXRD pattern (Fig. 2) that can be used to validate the purity and reproducibility of the synthesis.

Crystal structure analysis

A detailed crystal structure analysis must be carried out to understand the key differences between the two polymorphs in terms of their crystal packing and non-covalent interactions, which in turn will allow us to explain the variations observed in their physicochemical properties.

Form II displays a crystal structure closely related to that of **form I** (ref. 41) crystallizing in the monoclinic system, space group $P2_1/c$, with one molecule of FUR and one molecule of ETZ

Fig. 2 PXRD patterns and IR spectra of the APIs used and the polymorphs obtained in this work.

Table 2 Molecular descriptors and crystallographic structural data for **FUR–ETZ** polymorphs

Descriptors	Form I	Form II
Formula	$C_{12}H_{11}ClN_2O_5S, C_9H_{11}NO_2$	
Molecular weight	495.93	
Molecular volume (Å^3)	240.6, 146.9 (387.5)	241.0, 147.3 (388.3)
ΔH_{fus} (J g^{-1})	113.68	113.67
Space group	$P2_1/c$	$P2_1/c$
a (Å)	13.1846(4)	16.6876(10)
b (Å)	9.8733(3)	9.9126(6)
c (Å)	17.1518(6)	14.9984(10)
α (°)	90	90
β (°)	95.776(2)	114.686(3)
γ (°)	90	90
V (Å^3)	2221.41(12)	2254.3(2)
Z/Z'	4/1	4/1
Density (g cm^{-3})	1.483	1.461
Packing coefficient (%)	69.2	68.3
Void space (%)	1.3	0
Lattice energy (kcal mol^{-1})	−43.33	−42.49

in the asymmetric unit. In fact, the comparative analysis of the asymmetric units reveals that the independent molecules of FUR and ETZ adopt remarkably similar conformations in the two polymorphs. Root-mean-square deviation (RMSD) values, computed using Mercury software, were 0.1075 Å for FUR and 0.0624 Å for ETZ, indicating only minor deviations in their molecular conformations. These differences fall well below the 0.375 Å RMSD threshold defined by Cruz-Cabeza *et al.* for conformational polymorphisms.[65] This conformational consistency between **form I** and **form II** is visually demonstrated in Fig. S2, which overlays the molecular geometry of each component across the two forms. Additional crystallographic parameters and relevant molecular descriptors for both forms are summarized in Table 2.

In both forms, the packing is dominated by strong, directional hydrogen bonds of the N–H···O and O–H···O types. The most significant supramolecular motif is a robust heterosynthon formed between the carboxylic acid group of FUR and the amide group of ETZ, described by an $R_2^2(8)$ graph set (Fig. 4a), which is a well-known and highly favourable supramolecular interaction in

pharmaceutical cocrystals.[66–68] This interaction generates discrete **FUR–ETZ** dimers that serve as the primary building units. Additionally, both polymorphs present two intramolecular hydrogen bonds and one halogen bond that enhance the cohesion between the dimers (Fig. 3a). The first hydrogen bond is located within the FUR molecule, between the amine (–NH) and the carbonyl oxygen (C=O), and the second occurs within ETZ, between the amide (–NH$_2$) and the ethoxy oxygen (–C–O–C–), both forming $R_1^1(6)$ motifs. The Halogen bond involves the fluorine atom (F···NH$_2$) as shown in Fig. 3a.

Each dimer is subsequently linked to a second one through an additional N–H···O hydrogen bond involving the sulphonamide group of FUR and the carbonyl oxygen of ETZ, giving rise to tetramers (Fig. 3b). The organization of the tetramers along the *b*-axis allow the formation of 1D columnar structures that are stabilized through H–N–H···O–S–O hydrogen bonds. Thus, the classical strong hydrogen bonds (N–H···O, O–H···O) govern the supramolecular hierarchy from dimers to tetramers and columns, forming the dominant packing in both polymorphs.
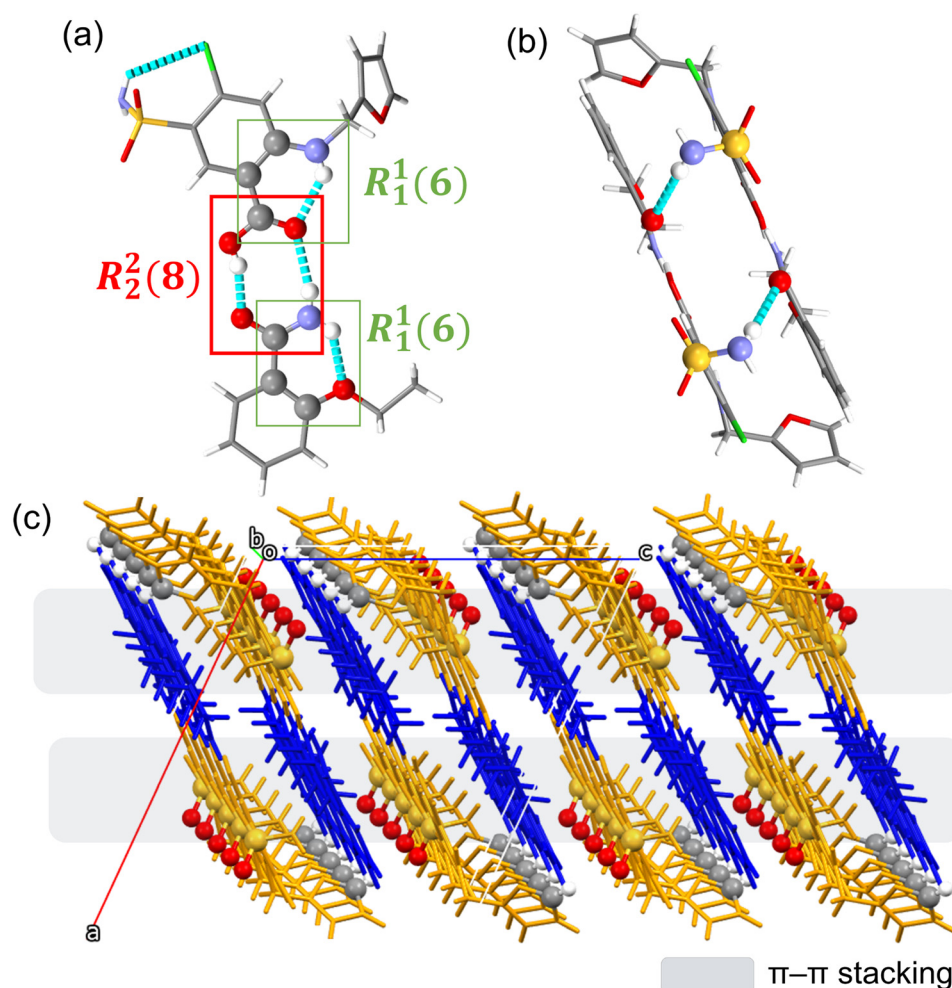

Fig. 3 (a) Asymmetric unit of **form II** and the H-bonds present within the cocrystal dimers. (b) Tetrameric formation in the crystal structure of **form II**. (c) Columnar organization along the *b* axis. In (c) ETZ molecules are represented in blue, while FUR molecules in orange. Atoms involved in the interactions are presented as balls and without colouring.
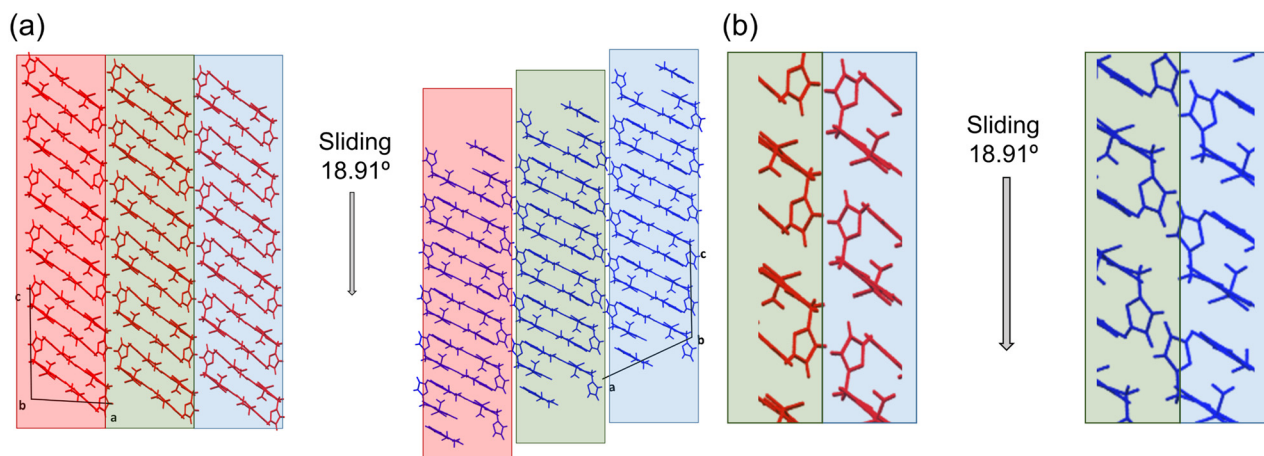
Fig. 4 (a) Layers of self-assembled **FUR–ETZ** molecules in **form I** (red) and **form II** (blue) of both polymorphs. Non-crystallographic translation of layers in **form II** respect to **form I** is shown through a highlighted fragment. The unit cell axes are schematically represented. (b) Detail of the sliding between two consecutive layers is also represented.

Beyond the primary 1D columnar arrangement, the 2D and 3D supramolecular architecture is consolidated by weaker interactions—notably C–H⋯O, C–H⋯π, and π⋯π contacts—that interconnect the columns. The C–H⋯O interactions, involving aromatic C–H donors and sulfonyl or carbonyl oxygen acceptors, bridge adjacent columns, while π⋯π stacking between aromatic rings further stabilizes the packing (Fig. 3c). The centroid–centroid distance for these π–π interactions is 3.73(17) Å, which is within the optimal range for effective aromatic stacking, improving the formation of the final 3D structure.

Despite their high degree of structural similarity, a key distinction between **form I** and **form II** lies in their crystal packing arrangements. Specifically, **form II** exhibits a non-crystallographic sliding of molecular layers relative to **form I**. This packing difference is highlighted in Fig. 4 and involves a lateral displacement of 18.91°, which results in a morphotropic transformation. This type of structural relationship—where one polymorph can be converted into another through simple layer rearrangements without altering the chemical composition or basic molecular conformation—falls under the category of morphotropism, as described by Kálmán.[69] This 18.91° sliding angle also corresponds to the difference observed in the β angle between the two forms at 298 K.

Computational studies

In addition to the crystal structure analysis, computational studies were conducted to gain deeper insight into the energetic and electronic factors governing the formation and stability of **form II**.

PBC calculations were applied to determine the lattice energies of both polymorphs, providing a direct comparison of their thermodynamic stability. We also utilized MEP surfaces of the individual coformers to explain the observed synthon preferences in each structure. A detailed analysis of key intermolecular interactions, particularly those involving

the furan moieties in FUR–FUR dimers, was conducted using QTAIM and NCI plot analysis. The differences in the crystal environment of each polymorph were analysed through Hirshfeld surface and its associated fingerprint plot analysis. Finally, BFDH morphologies of each polymorph were calculated to detect significant differences in the crystal surface.

PBC calculations were performed using the DMol3 software within the Materials Studio package, employing the PBE/dnp level of theory. To compute the lattice energy, a supercell containing 16 molecules (8 of each coformer) was constructed and its energy was compared to that of the unbound crystals. The resulting lattice energy for the previously reported cocrystal, **form I**, was found to be 20.5 kcal mol^{-1}, while **form II** exhibited a lattice energy of 20.7 kcal mol^{-1}. These results suggest that the two polymorphs possess an almost identical thermodynamic stability.

To understand the intermolecular interactions and synthon formation, we computed the Molecular MEP surfaces for the individual FUR and ETZ molecules (Fig. 5). The MEP surface for FUR shows a maximum at the carboxylic hydrogen
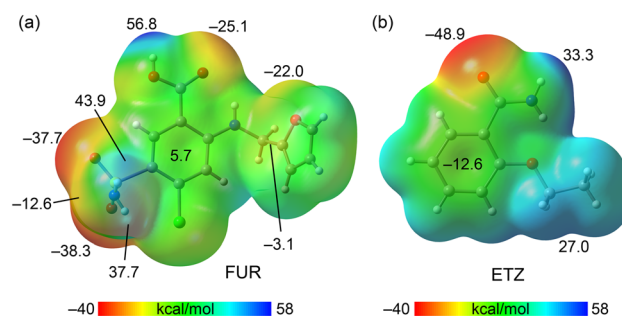

Fig. 5 MEP surfaces of (a) FUR and (b) ETZ calculated at the PBE0-D4/def2-TZVP level of theory. The colour scale ranges from −40 kcal mol^{-1} (red) to 58 kcal mol^{-1} (blue). Selected MEP values in kcal mol^{-1} for key sites on each molecule are indicated.

atom (56.8 kcal mol^{-1}), with other significant positive regions at the hydrogen atoms of the sulfonamide group (43.8 and 37.7 kcal mol^{-1}). The MEP is also positive over the aromatic six-membered ring (5.7 kcal mol^{-1}) and negative over the furan ring (−3.1 kcal mol^{-1}). The MEP minima are located at the oxygen atoms of the sulfonamide group (−37.7 and −38.3 kcal mol^{-1}), followed by the oxygen of the carboxylic group (−25.1 kcal mol^{-1}), the oxygen of the furan ring (−22.0 kcal mol^{-1}), and the nitrogen atom of the sulfonamide group (−12.6 kcal mol^{-1}). For ETZ, the MEP surface exhibits a maximum at the hydrogen atom of the amido group that is not involved in an intramolecular hydrogen bond (33.3 kcal mol^{-1}), followed by the aliphatic hydrogen atoms (27.0 kcal mol^{-1}). The MEP minimum is located at the oxygen atom of the amide group (−48.9 kcal mol^{-1}), and the MEP is negative over the aromatic ring (−12.6 kcal mol^{-1}). This analysis confirms that both molecules are rich in hydrogen bond donor and acceptor groups. Furthermore, the contrasting MEP values over the aromatic six-membered rings, positive for FUR and negative for ETZ, suggest that the formation of electrostatically enhanced π-stacking interactions between the coformers is highly favourable.

Fig. 6 illustrates three representative dimers extracted from the crystal structures. For the hydrogen-bonded dimers, we utilized the QTAIM to identify bond critical points (BCPs) and bond paths, which are represented as fuchsia spheres and dashed lines, respectively. For the π-stacking dimer, NCI plot analysis was employed, as it is more suitable for visualizing noncovalent interactions in real space, shown as an extended green isosurface.

The first type of dimer, shown in Fig. 6a and b, is a hydrogen-bonded assembly generated by an $R_2^2(8)$ synthon between the carboxylic acid of FUR and the amino group of ETZ. QTAIM analysis confirms two strong hydrogen bonds, O–H⋯O and N–H⋯O, each with a corresponding BCP and bond path. The dimerization energies for this assembly are similar for both polymorphs, with values of −12.6 kcal mol^{-1} for **form I** and −12.0 kcal mol^{-1} for **form II**, suggesting a slight energetic preference for this common synthon in **form I**. The second hydrogen-bonded assembly, Fig. 6c and d, is a homodimer involving the sulfonamide group of FUR as a hydrogen-bond donor and the oxygen atom of the furan ring as an acceptor. QTAIM analysis confirms the presence of N–H⋯O hydrogen bonds, as well as N–H⋯N and C–H⋯O
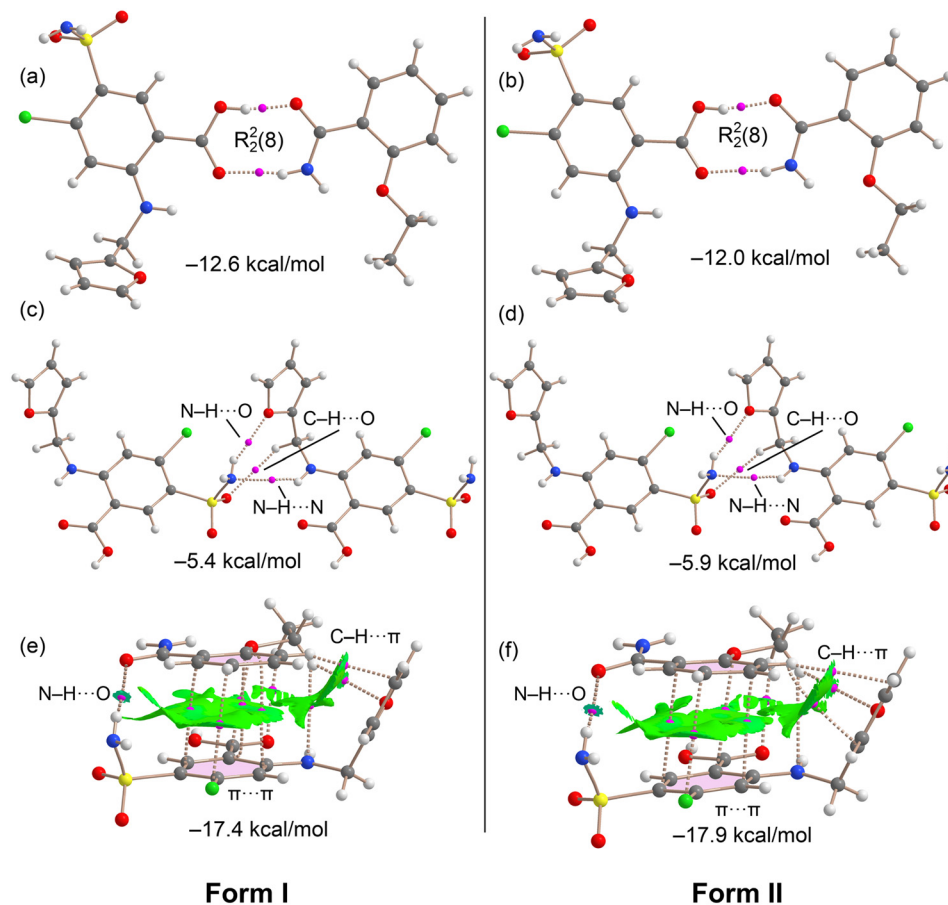

Fig. 6 Three representative dimers extracted from the crystal structures of **form I** (left column) and **form II** (right column) with their corresponding dimerization energies. (a and b) H-bonded dimers formed by an $R_2^2(8)$ synthon between FUR and ETZ. (c and d) H-bonded homodimers of FUR involving the sulfonamide and furan moieties. (e and f) π-stacking dimers between FUR and ETZ. BCPs represent QTAIM analysis in fuchsia spheres and bond paths as dashed lines. NCIplot scale is −0.035 ≤ (sign λ_2)ρ ≤ 0.035 a.u. only intermolecular interactions are represented.

contacts, indicated by the distribution of BCPs and bond paths. The dimerization energies for this homodimer are −5.9 kcal mol^{-1} for **form I** and −5.4 kcal mol^{-1} for **form II**, indicating a slightly stronger interaction in **form I**.

Finally, the π-stacking dimers, depicted in Fig. 6e and f, are formed between the two coformers. These assemblies are characterised by a large number of BCPs and bond paths that connect the molecules. The NCI plot reveals an extended and green reduced density gradient (RDG) isosurface, characterizing π-stacking between the six-membered aromatic rings, which aligns well with our MEP surface analysis. The analysis also reveals C–H⋯π interactions between aliphatic hydrogen atoms and the furan ring, as well as an N–H⋯O hydrogen bond between the sulfonamide N–H group and the oxygen atom of the ETZ amino group, characterized by a disk-shape RDG isosurface. The dimerization energies for these assemblies are notably large: −17.4 kcal mol^{-1} for **form I** and −17.9 kcal mol^{-1} for **form II**. These significant energies indicate that this assembly provides the dominant stabilization in both polymorphs. Interestingly, **form II** is more energetically favoured in this specific interaction, which partially compensates for the higher stability of the hydrogen-bonded dimers in **form I**. The overall similarity of the three dimer types across both polymorphs is remarkable. Fig. S3 illustrates the π-stacking dimers connected via the furan rings in both polymorphs.

In contrast to the assemblies shown in Fig. 6, these dimers have distinctly different geometries. For **form I**, the furan rings are π-stacked in an antiparallel face-to-face arrangement. This interaction is characterized by two BCPs interconnecting carbon atoms of the furan rings and a large RDG isosurface that encompasses most of the π-system. Conversely, in the new **form II**, the furan rings are parallel displaced with no π-system overlap. The interaction in **form II** is better described as a double C–H⋯π interaction, with a BCP and bond path connecting a hydrogen atom of the alkyl chain to a carbon atom of the furan ring. The interaction energy is 0.7 kcal mol^{-1} stronger in **form II**, which further contributes to compensating for the more favoured hydrogen-bonded dimers in **form I**. The interaction energies for these tetrameric assemblies were calculated by treating the π-stacked dimer as a monomer.

Overall, the π-stacking dimer in Fig. 6f and the furan⋯furan interaction shown in Fig. S3b for the new polymorph can compensate for the more favoured hydrogen-bonded dimers in **form I**, resulting in an overall higher stabilization for **form II** of only 0.1 kcal mol^{-1}. This result is in good agreement with the PBC calculations, which showed **form II** to be 0.2 kcal mol^{-1} more stable. In any case, this small difference, which is within the error margin of the computational method, confirms that both polymorphs are essentially isoenergetic.

Hirshfeld surface analysis and associated fingerprint plots were generated (Fig. 7 and S4–S8 further information), following the methodologies outlined by Spackman et al.[70–72] The analysis was conducted at three structural levels: individual molecules, asymmetric units, and the entire unit cell.
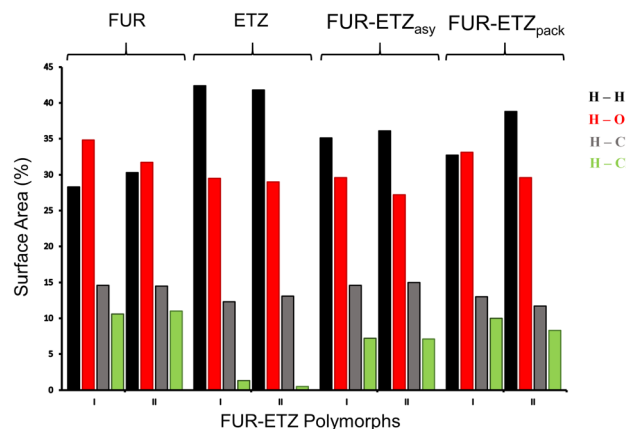

Fig. 7 Contribution (%) of intermolecular contacts of **forms I** and **II** calculated through Hirshfeld surfaces fingerprint plots: individual molecules, asymmetric unit and packing of both polymorphs.

First, similar intermolecular contacts occur in the individual molecules of FUR and EZT in both crystalline forms, presenting a greater contribution of H⋯O contacts in the FUR molecule of **form I** (34.8% versus 31.7%) and being slightly lower the contribution in the H⋯H contacts. The main contribution of the contacts present in ETZ molecules is the H⋯H interactions due to the strong acid–amide interaction and the intra –NH⋯OEt interaction that limits the formation of other intermolecular contacts. In the second approach, asymmetric unit surfaces were analyzed and secondary H⋯O contact corresponding to a sulphonamide–amide interaction was observed, showing the same global contact contributions in both polymorphs. Finally, in order to explore the packing environment, unit cell packing was analyzed displaying remarkable differences, especially in H–H contacts, showing the highest contribution in **form II** (38.8% versus 32.7%). On the other hand, H–O contacts have the highest contribution in **form I** and they are 3.5% more important than in **form II**. Hirshfeld surfaces suggest that although conformational adjustments are observed between both polymorphs, the crystal environment in the molecule of FUR affects the packing environment, showing differences in the global contribution of intermolecular contacts (Fig. 8).

The greater proportion of H⋯O contacts in **form I** highlights the formation of a stronger and more cooperative hydrogen-bonding network, resulting in a higher packing coefficient (69.2% vs. 68.3%), density (Table 2). By contrast, the dominance of H⋯H contacts in **form II** points to a less efficient packing, largely stabilized by weaker dispersive interactions. Furthermore, repulsive Cl⋯Cl contacts are observed in **form II** caused by the shortest distance between Cl atoms (3.67 Å). In **form I**, the distance between Cl atoms is 6.32 Å, therefore the Cl⋯Cl contact is not possible, leaving the void spaces present during packing (Fig. S8). The short Cl⋯Cl contacts in **form II** introduce local repulsive strain absent in **form I**, where larger Cl–Cl separations prevent destabilizing interactions.
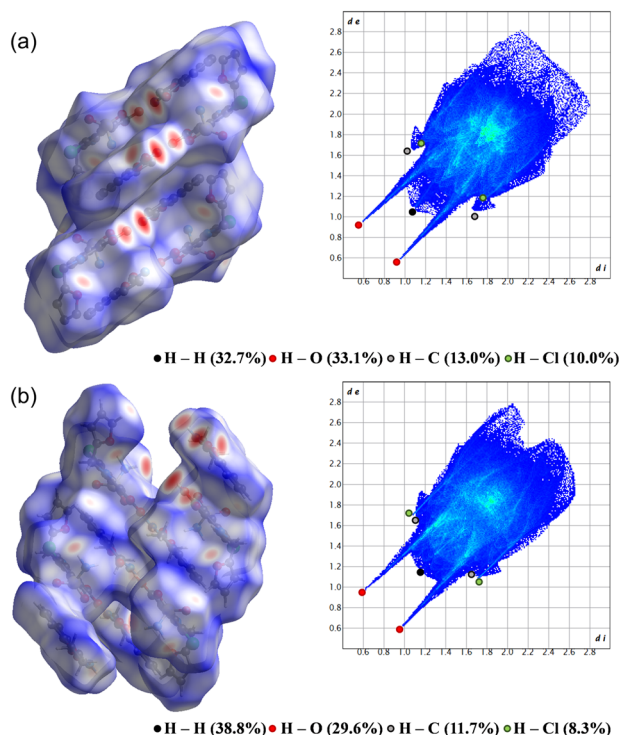
● H – H (32.7%) ● H – O (33.1%) ○ H – C (13.0%) ○ H – Cl (10.0%)

● H – H (38.8%) ● H – O (29.6%) ○ H – C (11.7%) ○ H – Cl (8.3%)

Fig. 8 Hirshfeld surface (left) and fingerprint plot (right) of **form I** (a) and **form II** (b) of the unit cell packing of the polymorphs of **FUR–ETZ** cocrystals. Main H–X contacts are highlighted in fingerprint plot figures.

Despite **FUR–ETZ** polymorphs are essentially isoenergetic, these features, together with the morphotropic sliding of molecular layers observed in **form II**, can be key factors that determine the most stable polymorph.

Aiming to detect significant differences in the crystal surface, which could predict possible variation in the solubility of the polymorphs, BFDH morphologies were calculated using the BFDH method included in the software package Mercury.[73] Interestedly, although the predicted morphologies of both polymorphs shows the same faces {100}, {011}, {11−1}, {110}, {002}, {10−2} with different relative % of the total surface (Fig. S9), in the case of **form II** (Fig. 9b) the predicted morphology shows both molecules pointing out of the {100} and {−100} faces (corresponding to 43% of the total surface), and both functional groups carboxylic acid (FUR) and amide (ETZ) are not well satisfied. On the other hand, in **form I** both molecules are self-assembled and only a sulphonamide functional group are located at {110} (corresponding to 6% of the total surface) of the predicted morphology, Fig. 9a.

Stability studies

A key aspect in the characterization of polymorphic forms is the assessment of their stability under various conditions. Fig. 10 shows the DSC traces of both forms to assess their thermal behaviour. Both polymorphs show a single endothermic phenomenon, which corresponds to melting, at 178 °C for **form**
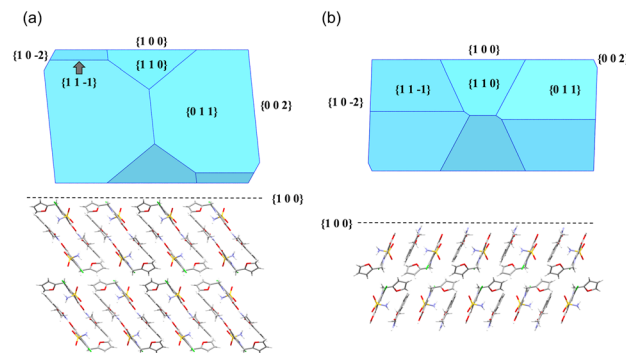

Fig. 9 BFDH predicted morphologies of **form I** (a) and **form II** (b), showing the faces (up). Morphologies filled with molecules of both polymorphs are represented (down) showing the respective packing according to their BFDH predicted morphologies.

I and at 182 °C for **form II**, followed by an exothermic phenomenon, which could be attributed to the decomposition of the cocrystal. However, the relative stability of both polymorphs according to Burger and Ramberger's heat of fusion rule[74] could not be studied because both polymorphs show the same enthalpy of fusion (113.7 J g^{-1}), (see SI Fig. S10 and S11 for further details). This marginal increase in the melting point temperature can be attributed to kinetic stabilisation *via* π–π stacking and hydrogen bonding in the columnar assemblies of **form II**, which, despite its metastable nature, may resist molecular motion up to a higher thermal threshold before decomposition.

Determining the relative thermodynamic stability of each polymorph is also essential to identify the most suitable form for further pharmaceutical development. Accelerated ageing conditions and aqueous solution (simulating physiologically relevant environments) were used for this purpose.

Accelerated ageing conditions, specifically at 40 °C and 75% RH, were selected following ICH guidelines for the evaluation of long-term stability in solid-state pharmaceutical materials.[75,76] Fig. S12 shows the PXRD patterns of both polymorphs during the exposure to these conditions (two months). No significant
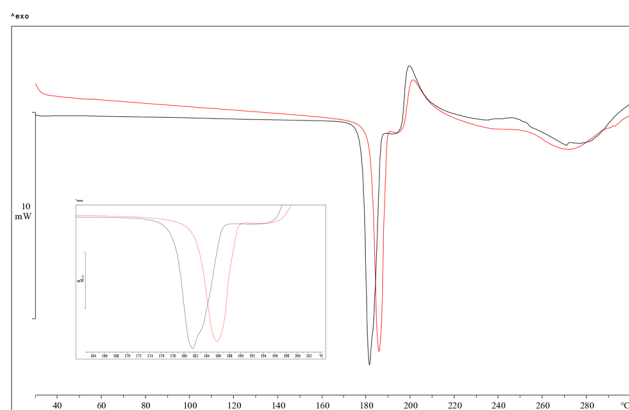

Fig. 10 DSC thermograms of **form I** (black) and **form II** (red) at a 10 °C min^{-1} heating rate. The events associated with the melting point are shown enlarged for greater detail.

changes were observed in the diffraction patterns, indicating that both polymorphs maintain their crystallinity and do not undergo polymorphic transitions, dissociation, or hydration over the study period. This result suggests that both solid forms are thermodynamically stable in the dry state under moderate thermal and humid stress.

While solid-state stability is crucial, it is also essential to assess the behaviour of the polymorphs upon contact with physiological fluids, particularly considering potential transformations after oral administration. For this reason, two pH values: PBS pH 6.8, mimicking the intestinal environment, and KCl pH 1.2 solution, representative of gastric conditions, were used.

Fig. S13 summarized the PXRD patterns obtained after 24 hours of suspension. In PBS solution, **form I** remained stable over 24 hours, with no detectable changes in the diffraction pattern. In contrast, **form II** exhibited partial transformation into **form I**. Additionally, the PXRD pattern of **form II** showed a broadening and reduction of signal intensity, suggesting a partial loss of crystallinity. This phenomenon is often observed in solid-state transitions where a metastable phase undergoes molecular reorganization toward a more stable polymorph, typically accompanied by a disordered intermediate phase.[77–79] The reduction in crystallinity is therefore indicative of a polymorphic transition in progress, rather than complete amorphization.[80,81]

Similar behaviour was observed in the acidic medium. **Form I** remained stable throughout the experiment, while **form II** again showed partial conversion to **form I** and signs of crystallinity loss. These observations further support the conclusion that **form I** is the more stable polymorph in aqueous environments across a broad pH range.

To further investigate the relative thermodynamic stability between the two polymorphs, a competition study was conducted. However, aqueous suspension was not feasible, as the sample formed a gelatinous, highly viscous mass, not allowing the formation of a homogeneous suspension and reducing the contact between solid phases, which is necessary for competence studies. In contrast, in MET and EOH, the cocrystals fully dissolved, eliminating the possibility of monitoring solid–solid transitions. Therefore, the study was performed in *n*-hexane, an apolar, non-interacting solvent chosen to minimise solubility and ensure a true solid-state transformation pathway.

Three experimental setups were designed: (i) suspension of **form I** (ii) suspension of **form II** and (iii) suspension of 1 : 1 physical mixture of **form I** and **form II**. All suspensions were maintained at room temperature under constant stirring and monitored over 15 days using PXRD.

Fig. S14 shows the results of the competence studies, where **form I** suspension revealed no detectable changes throughout the 15 days.

The consistent and sharp reflections indicate that **form I** is thermodynamically stable under these conditions, with no evidence of transformation or degradation, again, supporting the role of **form I** as the most energetically favourable

polymorph. In contrast, **form II** showed clear signs of polymorphic transformation. After 48 hours of suspension, characteristic peaks of **form I** began to emerge. These signals progressively intensified over 15 days, ultimately resulting in a polymorphic mixture, where **form I** and **form II** coexist. Notably, PXRD patterns obtained within the first 24 hours of all samples showed a temporary reduction in overall crystallinity. This effect was particularly evident in **form II** and the 1 : 1 mixture. As commented before, the temporary broadening and decrease in peak intensities suggest partial amorphization, which likely facilitates molecular rearrangement necessary for the phase transition.

The 1 : 1 mixture of **form I** and **form II** the transformation of **form II** into **form I** was more pronounced. After 5 days, no observable changes in the PXRD pattern were observed. Although a complete conversion was not observed, PXRD data showed a decline in the intensity of **form II** reflections, with near-complete disappearance of its peaks after 15 days, indicating a final stage of equilibrium in which both polymorphs coexists in suspensions, with a major predominance of the more stable **form I**. This supports the Ostwald rule of stages[82] and suggests that **form II**, while kinetically accessible, is metastable and undergoes a slow but spontaneous transformation toward the more stable form under these conditions. This slow conversion is a direct consequence of the crystal structure features observed in SCXRD, along with the results of our computational studies.

Solubility studies

Solubility studies were conducted to evaluate differences in the solubility profiles of the two polymorphs and to understand how crystal packing and structural features influence in this property. Quantification of **FUR** and **ETZ** was performed using HPLC, as their UV–Vis absorption spectra overlap, making conventional spectrophotometric analysis unsuitable.

The results presented in Table 3 showed that cocrystallization of FUR with ETZ tripled the solubility of the parent APIs. Both polymorphs displayed comparable solubility values, with **form II** exhibiting a slightly higher solubility than **form I**. Compared to the pure APIs, under physiological conditions (PBS, pH 6.8) the solubility of **FUR** increased nearly threefold, while under acidic conditions (KCl, pH 1.2) the solubility of **FUR** in the cocrystal was approximately four times higher than that of the free drug. For **ETZ**, the cocrystal

Table 3 Solubility of FUR and ETZ in mg mL^{-1} obtained by the FUR–ETZ polymorphs and the parent APIs in both, buffer PBS (pH 6.8) and KCl (pH 1.2)

Compound	PBS pH 6.8		KCl pH 1.2	
	FUR	**ETZ**	**FUR**	**ETZ**
Form I	0.886	0.331	0.004	0.049
Form II	1.078	0.356	0.004	0.053
FUR	0.352	—	0.001	—
ETZ	—	0.116	—	0.056

exhibited approximately threefold improved solubility in PBS, whereas under acidic conditions, the solubility was comparable to that of the native API.

Despite their similarities in crystal packing, the differences in the surface morphology simulations indicated that **form II** exposes a greater proportion of polar functional groups on the dominant {±100} faces, which is directly related to the water solubility.[83] Additionally, the higher contribution of H···H contacts and a lower proportion of H···O interactions compared to **form I**, together with the presence of short Cl···Cl repulsive contacts, results in a less efficient packing. This arrangement, in combination with a more polar surface due to the exposure of carboxylic acid and amide groups on the predominant crystal faces facilitates stronger interactions with water molecules, improving the solubility of **form II**.

Conclusions

In this study, we have identified, isolated, and characterized a novel polymorph of the **FUR–ETZ** cocrystal, only accessible *via* kinetic crystallization methods. The further characterization *via* SCXRD revealed that both polymorphs exist are quasi-isostructural forms with a morphotropic relationship, produced by a non-crystallographic translation within their crystal structures.[84] In fact, this study represents, to the best of our knowledge, the first report of a cocrystal exhibiting both morphotropism and concomitant crystallization. This unique combination establishes the **FUR–ETZ** system as a promising model for studying this intriguing and pharmaceutically relevant phenomenon.

Computational analyses provided further insight into the intermolecular forces governing the formation and stability of the two polymorphs. PBC calculations revealed that **form I** and **form II** are essentially isoenergetic. A detailed analysis of key dimers extracted from the crystal structures, using QTAIM and NCIplot, showed that while **form I** benefit from slightly stronger hydrogen-bonded interactions, **form II** is stabilized by enhanced π–π stacking, particularly in the furan···furan assemblies. Complementary Hirshfeld surface and fingerprint plot analyses confirmed these trends, with **form I** showing a greater proportion of strong H···O contacts that promote compact and cohesive packing, whereas **form II** exhibits a higher contribution of weaker H···H interactions and short Cl···Cl repulsive contacts.

These features indicate less efficient packing and increased surface polarity, which together explain both the gradual transformation, observed only in aqueous media, of **form II** into **form I** as well as the relatively higher solubility of **form II** compared to **form I** and the parent APIs. Thus, **form II** cannot be regarded as a viable option for pharmaceutical applications due to its metastable character.

Our findings emphasize the importance of systematic solid-form screening, as even subtle structural variations in packing and intermolecular interactions can decisively impact stability, solubility, and pharmaceutical performance.

Author contributions

D. C.-L. designed the experiments. D. C.-L. supervised the project. E. M.-H, C. A.-P., A. D.-M., R. P., A. F., R. B. and F. J. A.-M. conducted the experiments and analyzed the data. D. C.-L. and F. J. A.-M. prepared the manuscript. Funding acquisition, D. C.-L. All authors revised the manuscript. All authors have read and agreed to the published version of the manuscript.

Conflicts of interest

There are no conflicts to declare.

Data availability

The data supporting this article have been included as part of the supplementary information (SI).

Supplementary information: PXRD patterns, Hirshfeld surfaces and fingerprints plots, BFDH relative areas, DSC curves and crystallographic plots. See DOI: https://doi.org/10.1039/d5ce00942a.

CCDC 2489369 (**form II**) contains the supplementary crystallographic data for this paper.[85]

Acknowledgements

References

1 S. N. Wong, Y. C. S. Chen, B. Xuan, C. C. Sun and S. F. Chow, *CrystEngComm*, 2021, **23**, 7005–7038.

2 K. T. Savjani, A. K. Gajjar and J. K. Savjani, *ISRN Pharm.*, 2012, **2012**, 1–10.

3 B. Homayun, X. Lin and H.-J. Choi, *Pharmaceutics*, 2019, **11**, 129.

4 J. B. Ngilirabanga and H. Samsodien, *Nano Sel.*, 2021, **2**, 512–526.

5 G. Bolla, B. Sarma and A. K. Nangia, *Chem. Rev.*, 2022, **122**, 11514–11603.

6 D. J. Berry and J. W. Steed, *Adv. Drug Delivery Rev.*, 2017, **117**, 3–24.

7 N. Rodríguez-Hornedo, *Mol. Pharmaceutics*, 2007, **4**, 299–300.

8 D. Yang, R. Wang, G. Jin, B. Zhang, L. Zhang, Y. Lu and G. Du, *Cryst. Growth Des.*, 2019, **19**, 6175–6183.

9 U. Garg and Y. Azim, *RSC Med. Chem.*, 2021, **12**, 705–721.

10 S. Aitipamula, P. S. Chow and R. B. H. Tan, *CrystEngComm*, 2014, **16**, 3451.

11 R. Censi and P. Di Martino, *Molecules*, 2015, **20**, 18759–18776.

12 A. J. Cruz-Cabeza, S. M. Reutzel-Edens and J. Bernstein, *Chem. Soc. Rev.*, 2015, **44**, 8619–8635.

13 S. D. Parent, P. A. Smith, D. K. Purcell, D. T. Smith, S. J. Bogdanowich-Knipp, A. S. Bhavsar, L. R. Chan, J. M. Croom, H. C. Bauser, A. McCalip, S. R. Byrn and A. Radocea, *Cryst. Growth Des.*, 2023, **23**, 320–325.

14 Q. Shi, H. Chen, Y. Wang, J. Xu, Z. Liu and C. Zhang, *Int. J. Pharm.*, 2022, **611**, 121320.

15 X. Liang, A. S. Larsen, P. Hans, D. Xu, Y. Li, I. C. B. Martins, T. Rades and Y. Jiang, *CrystEngComm*, 2025, **25**, 6415–6432.

16 K. Linberg, B. Röder, D. Al-Sabbagh, F. Emmerling and A. A. L. Michalchuk, *Faraday Discuss.*, 2023, **241**, 178–193.

17 F. Fischer, A. Heidrich, S. Greiser, S. Benemann, K. Rademann and F. Emmerling, *Cryst. Growth Des.*, 2016, **16**, 1701–1707.

18 J. A. Baptista, R. A. E. Castro, M. T. S. Rosado, T. M. R. Maria, M. R. Silva, J. Canotilho and M. E. S. Eusébio, *Cryst. Growth Des.*, 2021, **21**, 3699–3713.

19 H. Liu, H. C. S. Chan, X. Yu, J. Li, J. Li and Z. Zhou, *Cryst. Growth Des.*, 2023, **23**, 4448–4459.

20 S. Aitipamula, A. B. H. Wong, P. S. Chow and R. B. H. Tan, *CrystEngComm*, 2013, **15**, 5877.

21 E. Sangtani, S. K. Sahu, S. H. Thorat, R. L. Gawade, K. K. Jha, P. Munshi and R. G. Gonnade, *Cryst. Growth Des.*, 2015, **15**, 5858–5872.

22 J. Zhang, Y. Jing, M. Wan, J. Xue, J. Liu, J. Li and Y. Du, *Spectrochim. Acta, Part A*, 2024, **305**, 123478.

23 L. Wang, Q. Xie, X. Shi, Y. Zhu, S. Li, F. Ji, J. Yu, D. Li and H. Zhang, *J. Mol. Struct.*, 2024, **1308**, 138124.

24 R. G. Gonnade and E. Sangtani, *J. Indian Inst. Sci.*, 2017, **97**, 193–226.

25 N. J. Babu, L. S. Reddy, S. Aitipamula and A. Nangia, *Chem. – Asian J.*, 2008, **3**, 1122–1133.

26 A. O'Sullivan, S. Kelly, S. Bhattacharya, K. M. Ryan, M. N. Collins and L. Padrela, *Int. J. Pharm.*, 2024, **663**, 124596.

27 J. Jin, S. Wu, Y. Ma, C. Dong, W. Wang, X. Liu, H. Xu, G. Long, M. Zhang, J. Zhang and W. Huang, *ACS Appl. Mater. Interfaces*, 2020, **12**, 19718–19726.

28 K. M. Steed and J. W. Steed, *Chem. Rev.*, 2015, **115**, 2895–2933.

29 D. D. Gadade and S. S. Pekamwar, *Adv. Pharm. Bull.*, 2016, **6**, 479–494.

30 B. Homayun, X. Lin and H.-J. Choi, *Pharmaceutics*, 2019, **11**, 129.

31 S. N. Wong, Y. C. S. Chen, B. Xuan, C. C. Sun and S. F. Chow, *CrystEngComm*, 2021, **23**, 7005–7038.

32 A. Raw, *Adv. Drug Delivery Rev.*, 2004, **56**, 397–414.

33 P. Sacchi, S. E. Wright, P. Neoptolemou, G. I. Lampronti, A. K. Rajagopalan, W. Kras, C. L. Evans, P. Hodgkinson and A. J. Cruz-Cabeza, *Proc. Natl. Acad. Sci. U. S. A.*, 2024, **121**(15), e2319127121.

34 S. M. Guthrie, D.-M. Smilgies and G. Giri, *Cryst. Growth Des.*, 2018, **18**, 602–606.

35 M. Kitamura, *Cryst. Growth Des.*, 2004, **4**, 1153–1159.

36 J. Nozawa, M. Sato, S. Uda and K. Fujiwara, *Commun. Phys.*, 2025, **8**, 134.

37 M. Kitamura, *CrystEngComm*, 2009, **11**, 949.

38 K. Suresh, T. Mehta, V. Thakrar and R. G. Sharma, *Cryst. Growth Des.*, 2025, **25**, 1282–1292.

39 L. Qi, C. Li, X. Cheng, H. Hao and C. Xie, *Cryst. Growth Des.*, 2024, **24**, 6196–6203.

40 K. Trzeciak, M. K. Dudek and M. J. Potrzebowski, *Chem. – Eur. J.*, 2024, **30**, e202402683.

41 F. Acebedo-Martínez, C. Alarcón-Payer, L. Rodríguez-Domingo, A. Domínguez-Martín, J. Gómez-Morales and D. Choquesillo-Lazarte, *Crystals*, 2021, **11**, 1339.

42 Bruker APEX4.

43 O. V. Dolomanov, L. J. Bourhis, R. J. Gildea, J. A. K. Howard and H. Puschmann, *J. Appl. Crystallogr.*, 2009, **42**, 339–341.

44 C. F. Macrae, I. J. Bruno, J. A. Chisholm, P. R. Edgington, P. McCabe, E. Pidcock, L. Rodriguez-Monge, R. Taylor, J. Van De Streek and P. A. Wood, *J. Appl. Crystallogr.*, 2008, **41**, 466–470.

45 *BIOVIA*, San Diego, CA, USA.

46 B. Delley, *J. Chem. Phys.*, 1990, **92**, 508–517.

47 M. J. Frisch, G. W. Trucks, H. B. Schlegel, G. E. Scuseria, M. A. Robb, J. R. Cheeseman, G. Scalmani, V. Barone, G. A. Petersson, H. Nakatsuji, X. Li, M. Caricato, A. V. Marenich, J. Bloino, B. G. Janesko, R. Gomperts, B. Mennucci, H. P. Hratchian, J. V. Ortiz, A. F. Izmaylov, J. L. Sonnenberg, D. Williams-Young, F. Ding, F. Lipparini, F. Egidi, J. Goings, B. Peng, A. Petrone, T. Henderson, D. Ranasinghe, V. G. Zakrzewski, J. Gao, N. Rega, G. Zheng, W. Liang, M. Hada, M. Ehara, K. Toyota, R. Fukuda, J. Hasegawa, M. Ishida, T. Nakajima, Y. Honda, O. Kitao, H. Nakai, T. Vreven, K. Throssell, J. A. Montgomery Jr., J. E. Peralta, F. Ogliaro, M. J. Bearpark, J. J. Heyd, E. N. Brothers, K. N. Kudin, V. N. Staroverov, T. A. Keith, R. Kobayashi, J. Normand, K. Raghavachari, A. P. Rendell, J. C. Burant, S. S. Iyengar, J. Tomasi, M. Cossi, J. M. Millam, M. Klene, C. Adamo, R. Cammi, J. W. Ochterski, R. L. Martin, K. Morokuma, O. Farkas, J. B. Foresman and D. J. Fox, *Gaussian 16, Revision C.01*, Gaussian, Inc., Wallingford CT, 2016.

48 C. Adamo and V. Barone, *J. Chem. Phys.*, 1999, **110**, 6158–6170.

49 F. Weigend and R Ahlrichs, *Phys. Chem. Chem. Phys.*, 2005, **7**, 3297–3305.

50 S. Grimme, J. Antony, S. Ehrlich and H. Krieg, *J. Chem. Phys.*, 2010, **132**, 154104.

51 S. F. Boys and F. Bernardi, *Mol. Phys.*, 1970, **19**, 553–566.

52 R. F. W. Bader, *J. Phys. Chem.*, 1990, 438.

53 J. Contreras-García, E. R. Johnson, S. Keinan, R. Chaudret, J. P. Piquemal, D. N. Beratan and W. Yang, *J. Chem. Theory Comput.*, 2011, **7**, 625–632.

54 T. A. Keith, *Aust. J. Optom.*, 2019, **102**(4), 437–439.

55 A. Glomme, J. März and J. B. Dressman, *J. Pharm. Sci.*, 2005, **94**, 1–16.

56 F. Fischer, G. Scholz, S. Benemann, K. Rademann and F. Emmerling, *CrystEngComm*, 2014, **16**, 8272–8278.

57 D. Hasa, G. Schneider Rauber, D. Voinovich and W. Jones, *Am. Ethnol.*, 2015, **127**, 7479–7483.

58 D. Cinčić, I. Brekalo and B. Kaitner, *Cryst. Growth Des.*, 2012, **12**, 44–48.

59 K. Linberg, P. Szymoniak, A. Schönhals, F. Emmerling and A. A. L. Michalchuk, *Chem. – Eur. J.*, 2023, **29**, e202302150.

60 A. M. Belenguer, G. I. Lampronti, N. De Mitri, M. Driver, C. A. Hunter and J. K. M. Sanders, *J. Am. Chem. Soc.*, 2018, **140**, 17051–17059.

61 A. P. Voronin, A. G. Ramazanova, A. V. Churakov, A. V. Vologzhanina, E. S. Kulikova and G. L. Perlovich, *Cryst. Growth Des.*, 2024, **24**, 9773–9789.

62 J. H. Lee, K. H. Kim, S. A. Ryu, J. Kim, K. Jung, K. S. Kang and T. Yamaguchi, *Pharmaceutics*, 2025, **17**, 928.

63 E. H. Lee, *Asian J. Pharm. Sci.*, 2014, **9**, 163–175.

64 B. K. Hodnett and V. Verma, *Processes*, 2019, **7**, 272.

65 A. J. Cruz-Cabeza and J. Bernstein, *Chem. Rev.*, 2014, **114**, 2170–2191.

66 I. Sarcevica, L. Orola, M. V. Veidis, A. Podjava and S. Belyakov, *Cryst. Growth Des.*, 2013, **13**, 1082–1090.

67 O. N. Kavanagh, G. Walker and M. Lusi, *Cryst. Growth Des.*, 2019, **19**, 5308–5313.

68 A. Vriza, I. Sovago, D. Widdowson, V. Kurlin, P. A. Wood and M. S. Dyer, *Digital Discovery*, 2022, **1**, 834–850.

69 A. Kálmán, *Acta Crystallogr., Sect. B:Struct. Sci.*, 2005, **61**, 536–547.

70 M. A. Spackman and D. Jayatilaka, *CrystEngComm*, 2009, **11**, 19–32.

71 M. A. Spackman and J. J. McKinnon, *CrystEngComm*, 2002, **4**, 378–392.

72 J. J. McKinnon, D. Jayatilaka and M. A. Spackman, *Chem. Commun.*, 2007, 3814.

73 R. Docherty, G. Clydesdale, K. J. Roberts and P. Bennema, *J. Phys. D: Appl. Phys.*, 1991, **24**, 89–99.

74 A. Burger and R. Ramberger, *Microchim. Acta*, 1979, **72**, 259–271.

75 O. González-González, I. O. Ramirez, B. I. Ramirez, P. O'Connell, M. P. Ballesteros, J. J. Torrado and D. R. Serrano, *Pharmaceutics*, 2022, **14**, 2324.

76 P. Sengupta, B. Chatterjee and R. K. Tekade, *Int. J. Pharm.*, 2018, **543**, 328–344.

77 V. P. Kolesov, *Thermochim. Acta*, 1995, **266**, 129–145.

78 C. Brandel, Y. Cartigny, N. Couvrat, M. E. S. Eusébio, J. Canotilho, S. Petit and G. Coquerel, *Chem. Mater.*, 2015, **27**, 6360–6373.

79 P. F. McMillan, O. Shebanova, D. Daisenberger, R. Q. Cabrera, E. Bailey, A. Hector, V. Lees, D. Machon, A. Sella and M. Wilson, *Phase Transitions*, 2007, **80**, 1003–1032.

80 Yu. V. Mnyukh, *Mol. Cryst. Liq. Cryst.*, 1979, **52**, 163–199.

81 O. Renier, G. Bousrez, G. V. Baryshnikov, V. Paterlini, V. Smetana, H. Ågren, R. D. Rogers and A.-V. Mudring, *J. Am. Chem. Soc.*, 2021, **143**, 20202–20206.

82 W. Ostwald, *Z. Phys. Chem., Stoechiom. Verwandtschaftsl.*, 1897, **22U**, 289–330.

83 R. Barbas, M. Font-Bardia, A. Frontera and R. Prohens, *Cryst. Growth Des.*, 2022, **22**, 590–597.

84 A. Kálmán and L. Fábián, *Acta Crystallogr., Sect. B:Struct. Sci.*, 2007, **63**, 411–417.

85 CCDC 2489369: Experimental Crystal Structure Determination, 2025, DOI: 10.5517/ccdc.csd.cc2pkd7x.